



# Tunable strain soliton networks confine electrons in van der Waals materials

Drew Edelberg¹, Hemant Kumar 62, Vivek Shenoy³, Héctor Ochoa1 and Abhay N. Pasupathy 61 and Abhay 61 and Abh

Twisting or sliding two-dimensional crystals with respect to each other gives rise to moiré patterns determined by the difference in their periodicities. Such lattice mismatches can exist for several reasons: differences between the intrinsic lattice constants of the two layers, as is the case for graphene on BN1; rotations between the two lattices, as is the case for twisted bilayer graphene<sup>2</sup>; and strains between two identical layers in a bilayer3. Moiré patterns are responsible for a number of new electronic phenomena observed in recent years in van der Waals heterostructures, including the observation of superlattice Dirac points for graphene on BN1, collective electronic phases in twisted bilayers and twisted double bilayers<sup>4-8</sup>, and trapping of excitons in the moiré potential9-12. An open question is whether we can use moiré potentials to achieve strong trapping potentials for electrons. Here, we report a technique to achieve deep, deterministic trapping potentials via strain-based moiré engineering in van der Waals materials. We use strain engineering to create on-demand soliton networks in transition metal dichalcogenides. Intersecting solitons form a honeycomb-like network resulting from the three-fold symmetry of the adhesion potential between layers. The vertices of this network occur in bound pairs with different interlayer stacking arrangements. One vertex of the pair is found to be an efficient trap for electrons, displaying two states that are deeply confined within the semiconductor gap and have a spatial extent of 2 nm. Soliton networks thus provide a path to engineer deeply confined states with a strain-dependent tunable spatial separation, without the necessity of introducing chemical defects into the host materials.

Our strain engineering for a transition metal dichalcogenide (TMD) homobilayer is illustrated conceptually in Fig. 1a. At zero strain, the layers will form a commensurate structure. When large tensile strain is applied to only the bottom layer, the lattice constants differ, resulting in an incommensurate structure. In general, large changes in electronic structure are caused when there are significant rearrangements to atomic positions within each layer. This happens when the lattice mismatch between layers is small, which corresponds to the intermediate case of not too large heterostrain. In this regime, atoms try to adjust to the new stacking landscape, forming commensurate regions at the expense of elastic energy<sup>13</sup>. These commensurate regions are separated by topological solitons<sup>14-16</sup>, which are also corrugated in the vertical direction. A lattice of such solitons has been observed in very-small-angle twisted bilayer graphene $^{17-19}$ . The electronic properties of individual solitons have been studied by transport<sup>20</sup> and tunnelling studies, and manipulation of individual solitons has been achieved using a probe tip<sup>21,22</sup>. Random networks of solitons have also been observed previously in a variety of bilayer graphene samples<sup>3</sup>.

Being able to create these solitons on demand opens up new possibilities for studying their formation, reversibility and strain-tunable properties. This requires the ability to tune the strain between two adjacent layers of the TMD controllably while imaging the result of this process over a single region of the sample. In our work, we overcame these experimental challenges by developing a new apparatus that allowed us to apply controllable, large uniaxial strain while simultaneously performing scanning tunnelling microscopy (STM) measurements. Our experiments were conducted on vacuum-cleaved single crystals of MoSe<sub>2</sub>, the ends of which were affixed to a strain bridge as shown in Fig. 1b,c (for details see Methods). It is often found that the exfoliation process results in several micrometre-sized flakes of monolayers that are not bound to the edges of the sample, as illustrated in Fig. 1d. On application of strain to the bridge, the top layer is only connected to the rest of the sample via van der Waals interactions, while the rest of the sample is uniformly strained, mimicking the situation in Fig. 1a. To identify this scenario, we scanned across the surface of the crystal until we found a monolayer on the top surface that was not attached to the lateral ends of the crystal (see Supplementary Fig. 1 for a topographic scan across the edge of one such monolayer). Such flakes were observed in 4 out of 15 samples studied in this experiment, with lateral sizes that were at least several micrometres (larger than the range of our STM scanner). We then scanned a large area  $(1.5 \times 1.5 \,\mu\text{m}^2)$  of this top layer far (more than  $1 \,\mu\text{m}$ ) from any edge. The resultant topographic scan, obtained at zero strain, is shown in Fig. 1e. This topograph is flat to within ~1 Å, with the residual roughness due to the presence of point defects in the crystal<sup>23</sup>. On increasing the strain beyond a critical value (determined to be ~1.5%), clear signs of the formation of strain solitons are seen in STM topographs. The density of solitons grows with applied strain, as shown in Fig. 1f,g, corresponding to strains of 2% and 3%, respectively. All three images (Fig. 1e-g) were obtained on exactly the same region of the sample. The process of soliton formation is reversible—on removal of the strain, the solitons disappeared and the system returned to its initial commensurate state. Some hysteresis was observed, but it is difficult to disentangle intrinsic hysteresis in the dynamics of the soliton lattice from hysteresis present in the piezoelectric elements used for strain tuning.

We next consider the atomic-scale structure of a single soliton (Fig. 2a). Each bright spot in this topograph corresponds to a Se atom on the surface of the top layer. The long axis of the soliton coincides with an armchair direction of the crystal. By taking a topographic line cut along the short zigzag axis, we can extract the height profile for the corrugation (Fig. 2b). The maximum apparent

LETTERS NATURE PHYSICS

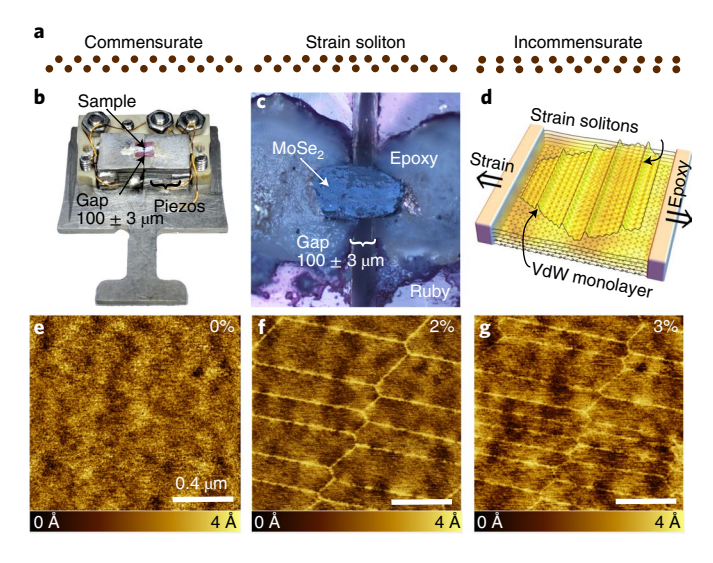


**Fig. 1** | **Strain soliton networks in MoSe<sub>2</sub>. a**, Schematics of the commensurate, partially incommensurate (strain solitons) and totally incommensurate bilayer structures. **b**, Piezoelectric-based device for performing STM measurements under large uniaxial strain. **c**, Optical image of a MoSe<sub>2</sub> crystal affixed across the two independent piezoelectric stacks. The sample is bonded to each stack by epoxy. **d**, Schematic of a free monolayer on the top surface of the crystal after cleaving in vacuum. Strain was transmitted only through the bulk material underneath. VdW, van der Waals. **e-g**, STM topographic images of a  $1.5 \times 1.5 \, \mu\text{m}^2$  region of the top monolayer at strains of 0% (**e**), 2% (**f**) and 3% (**g**) ( $V = 0.8 \, \text{V}$ ,  $I = 100 \, \text{pA}$ ). Before applying strain, the residual height variations are due to crystal defects. Above a critical strain of 1.5%, solitons begin to form, increasing in density as strain increases.

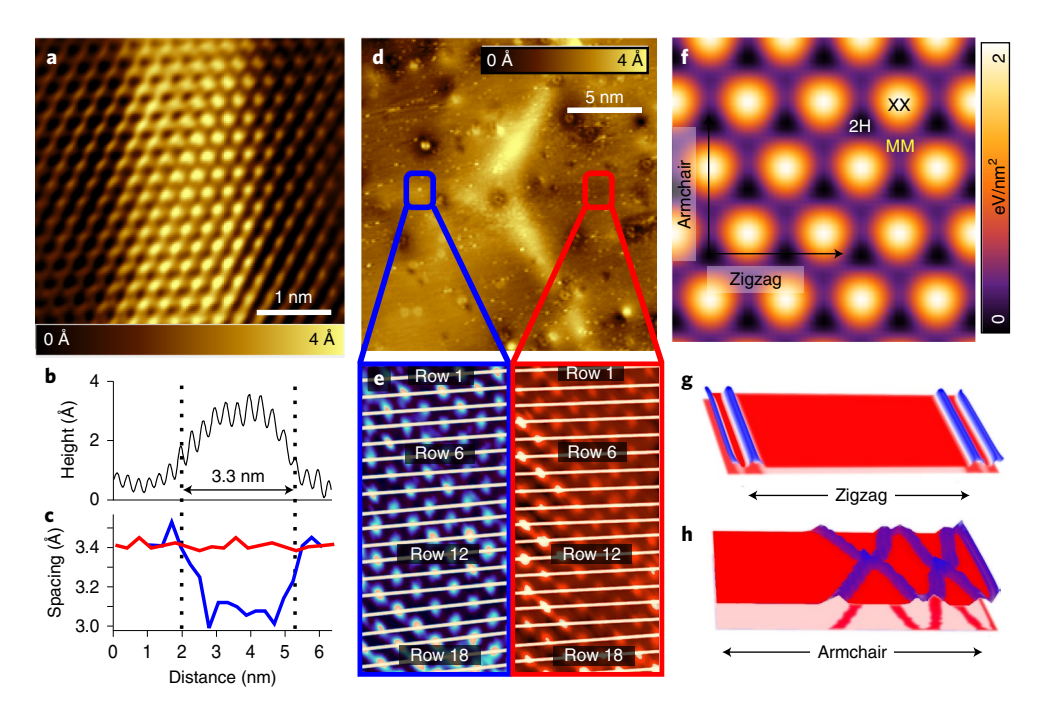


**Fig. 2 | Atomic structure of a single soliton. a**, Atomically resolved STM topographic image (V=1V, I=100 pA) of one of the solitons, where the top lattice of Se atoms is well resolved. **b**, Height profile across the soliton, extracted from **a**. **c**, Local lattice spacing (projected on the horizontal plane) across the soliton (blue line) and in the background region (red line). In the soliton region, the local lattice spacing is reduced, corresponding to a release of tensile strain in the top layer. **d**, Topographic image of three solitons crossing at a vertex. The lattice spacings on and off the soliton shown in **c** come from the regions bounded by the blue and red boxes, respectively. **e**, Excerpts from **d** showing atomic resolution on (blue) and off (red) a soliton. A count of atoms across the soliton contains one extra atomic row, indicating a discommensuration of one lattice spacing across the soliton. **f**, Free-energy landscape of stacking configurations (for details of the calculation see Supplementary Section 2). **g,h**, Soliton solutions deduced from our numerical simulations when strain is applied along the zigzag (**g**) and armchair (**h**) directions.

height was measured to be 3 Å, with a lateral width of 3.3 nm. We can also use the distance between adjacent peaks and troughs in atomically resolved topographs to estimate the local lattice constant. The blue curve in Fig. 2c represents the local interatomic distance

recorded across a soliton, while the red curve is the lattice constant in a region without a soliton; both regions are highlighted in Fig. 2d. In the line cut without the soliton, the average lattice spacing is ~3.4 Å, consistent with a MoSe<sub>2</sub> layer under tensile strain.

NATURE PHYSICS LETTERS

The lattice spacing at the soliton centre is smaller, ~3.05 Å, indicating that stress is relieved. The integrated difference in lattice spacing across the soliton is found to be near one lattice constant. We can further confirm this by counting atomic rows parallel to the soliton in the blue and red regions. Figure 2e shows side-by-side comparisons of the corresponding topographic excerpts. The region across the soliton contains exactly one extra atomic row, implying that the corrugation is a discommensuration of one lattice spacing along a zigzag axis.

The preferential direction of solitons separating different commensurate areas can be understood from the symmetry of the adhesion potential shown in Fig. 2f (for details of the calculation see Supplementary Section 2). The minimum of this potential corresponds to the hexagonal (2H) stacking of the bulk material, while the maximum corresponds to a configuration where Se atoms lie on top of each other (XX); the configuration with transition-metal sublattices sitting on top of one another (MM) is a local minimum, close in energy to a saddle point (the stacking at the centre of the soliton). Away from the solitons, the system is in the 2H stacking configuration (darkest areas, Fig. 2f). Going across a single soliton therefore corresponds to moving from one 2H potential minimum to a nearby one. Moving along the zigzag direction (horizontal arrow, Fig. 2f) avoids XX stacking configurations (brightest areas, Fig. 2f), resulting in a lower energy cost. This is also borne out in our finite-element method simulations for soliton formation shown in Fig. 2g,h. Tensile heterostrain applied along the zigzag direction results in the formation of solitons along the perpendicular direction. For tensile heterostrain along the armchair direction, the resulting solitons are still perpendicular to zigzag directions, along which stress is relieved.

Based on this potential landscape, the critical strain for the formation of solitons can be estimated as (Supplementary Section 3)

$$\bar{u}_{\rm c} = \frac{\eta_{\varphi} 8}{\pi} \sqrt{\frac{V}{\lambda + 2\mu}} \approx 1.7 - 2\% \tag{1}$$

where  $\lambda$  and  $\mu \approx 3\,\mathrm{eV}\,\mathrm{Å}^{-2}$  are the Lamé coefficients of the monolayer<sup>24</sup>,  $V \approx 43\,\mathrm{meV}\,\mathrm{nm}^{-2}$  is the scale characterizing the free-energy difference between stacking configurations, and  $\eta_{\varphi}$  is a numerical factor depending on the orientation of the sample ( $\eta_0 = 1$  if the tension is along a zigzag axis,  $\eta_{\pi/6} \approx 1.22$  in the case of an armchair direction). The soliton width is

$$\ell = \frac{\tilde{a}}{4\pi} \sqrt{\frac{\lambda + 2\mu}{V}} \approx 4 \text{ nm}$$
 (2)

where  $\tilde{a} \approx 3.4 \, \text{Å}$  is the lattice constant of strained MoSe<sub>2</sub>. The critical strain  $\bar{u}_c$  decreases with temperature<sup>25</sup>, which is not considered in our estimates. Moreover, both thermal fluctuations and disorder break positional long-range order in the soliton system. Pinning by lattice defects is not efficient, as the solitons are extensive objects and the range of these forces is likely to be only atomistic. Nevertheless, disorder can also create inhomogeneous distributions of strain, favouring the appearance of dislocations in the soliton system. A large-scale image of one of these dislocations is shown in Supplementary Fig. 2. Additionally, the three-fold symmetry of the adhesion potential (only weakly broken by the uniaxial strain) implies the existence of more than one easy direction for the solitons. Even at low temperatures and despite the energy cost of soliton crossings, thermal fluctuations can stabilize two-dimensional (2D) networks as these structures carry large configuration entropy.

We next consider the formation and properties of soliton crossings. Figure 3a-c shows a sequence of STM images over the same region of the sample at strains of 1.8%, 2.0% and 2.2%, respectively. At the smallest of these strains, solitons are already formed

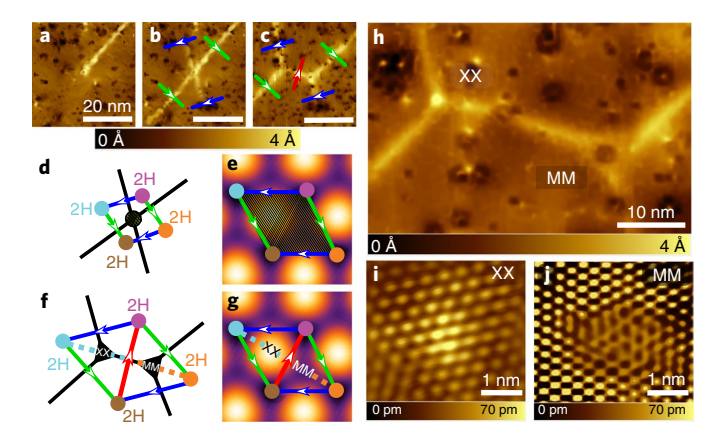
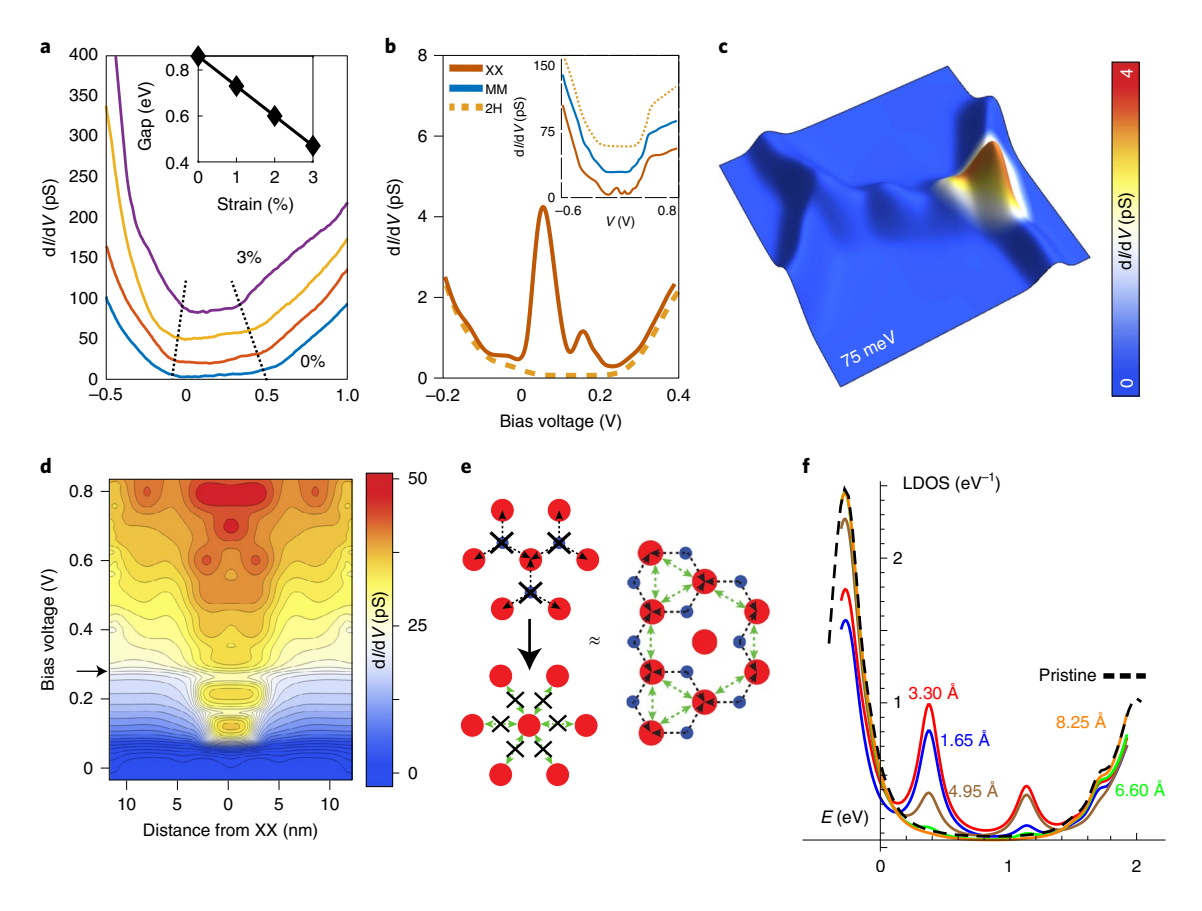


Fig. 3 | Soliton crossings and vertices. a-c, STM topographic images (V=1V, I=50 pA) at strains of 1.8% (a), 2.0% (b) and 2.2%(c), showing the evolution from a pinned soliton endpoint (a) to formation of a second soliton with a soliton crossing (b) to splitting of the soliton crossing into two vertices (c). d, Schematic of the soliton crossing in b. e, Corresponding path of the system in configuration space in the various regions. Across each of the solitons, the system transits from one 2H minimum to a neighbouring one, as indicated by the green and blue coloured arrows. In the region of the crossing, the system explores all possible stacking configurations, including XX and MM extremes. f, Schematic of the two vertices in c. g, Corresponding path of the system in configuration space. Paths (blue and orange dashed lines) connecting commensurate regions with the third soliton (red arrow) indicate how the two vertices correspond to XX and MM stackings. **h**, STM topographic image (V=1V, I=50 pA) of a short soliton connecting to two vertices with XX and MM stacking configurations. i,j, STM topographic images (V=1V, I=50 pA) of the XX (i) and MM (j) soliton vertices. For the XX soliton in i, the topographic height decays quickly on the atomic scale. For the MM soliton vertex in j, the triangular lattice is blurred on a longer length scale, replaced by a honeycomb pattern at the centre of the crossing.

in stripes. Figure 3a shows the endpoint of one of these solitons, corresponding to the core of a dislocation in the stripe order. On increasing the strain (Fig. 3b), a new soliton nucleates, forming an intersection where discommensurations along two zigzag directions coincide. On increasing the strain further (Fig. 3c), the soliton crossing is seen to split into two separate vertices where three solitons meet. A consideration of how the stacking order evolves across soliton crossings can help us to understand the splitting of the initial intersection into two three-fold vertices. Shown in Fig. 3d is a schematic of the soliton crossing of Fig. 3b. Each of the solitons corresponds to a phase slip of one lattice constant along the green and blue arrow directions, respectively. The corresponding paths in the configuration space of stacking orders are visualized by arrows of the same colours in Fig. 3e; the soliton crossing itself corresponds to the shaded region, where all stackings are sampled, resulting in a high energy cost. This soliton crossing is therefore unstable and relaxes quickly (shown in Fig. 3c) into two separate vertices connected by a third soliton. The schematic for this image and the corresponding paths in configuration space are shown in Fig. 3f,g. The formation of the honeycomb-like soliton network or a multi-domain stripe phase as seen in Fig. 1 is a consequence of these relaxation processes.

The two separate vertices have rather different properties. Consider the configuration of the system as one traverses along the soliton across each of the two vertices (blue and orange dashed lines, Fig. 3f). The corresponding path in configuration space is shown by the dashed lines in Fig. 3g. For one of the intersections (blue dashed line), going across the soliton vertex results in the

LETTERS NATURE PHYSICS



**Fig. 4 | Spectroscopic properties of soliton vertices. a**, STS spectra recorded on bulk MoSe<sub>2</sub>. The indirect gap closes as the strain grows. The dependence of the gap on strain is shown in the inset. **b**, LDOS within the semiconducting gap recorded on an XX soliton crossing (solid line) and commensurate 2H region (dashed line) at a strain of 2.5%. The XX vertices display clear midgap states. The inset shows the LDOS on larger energy scales, also showing that the MM soliton crossing does not display midgap states. Additionally, the spectra at both vertices display smaller resonances in the semiconductor bands, which are more clearly resolved in the conduction band. **c**, 3D spectroscopic image in the region of the two soliton crossings at  $V = 75 \,\text{mV}$ , corresponding to the energy of the lower bound state in **b**. The 3D height in this image is the topographic height of the tip, showing the location of the MM and XX soliton crossings. The colour scale is the magnitude of the differential conductance, showing that the resonance is localized in the vicinity of the XX soliton crossing while the rest of the area is gapped. **d**, Angular-averaged STS maps in the conduction band around an XX crossing. The conduction band edge is indicated by the arrow on the y axis. The resonances in the conduction band have alternating odd-even parity, as expected for a harmonic oscillator. The two midgap states do not follow this sequence. **e**, Model for a stacking defect on an XX soliton vertex: passivation of the Se (blue) orbitals due to a strong interlayer coupling interrupts the effective hopping between Mo (red) orbitals, which dominate the low-energy bands, leading to an effective vacancy. **f**, Calculated density of states at different distances from the stacking defect for a monolayer (for details of the model and calculation see Supplementary Section 7).

system going through the XX stacking configuration, while for the other soliton vertex the system goes through the MM stacking configuration. We term these the XX and MM vertices, respectively. We imaged several of these shorter solitons with STM with high resolution (one representative example is shown in Fig. 3h). The two vertices show a distinct topographic contrast (one brighter or higher than the other), which was systematically reproduced over the sample. Figure 3i,j shows atomic-resolution images taken at each vertex. Figure 3i shows a triangular pattern at the bright vertex, the apparent height of which decays fast on the atomic scale. This suggests that Se atoms are lifted by the local XX stacking in this region, and therefore are lifted with respect to the surrounding commensurate regions. In contrast, at the darker vertex (Fig. 3j), the topographic contrast resembles two interpenetrating triangular lattices, resulting in a honeycomb geometry. A plausible reason for this is that the Mo atoms in this region are pushed upward by the local MM stacking, allowing them to be visible in the topograph. This identification of the two vertices based on local topography is also compatible with our previous observation that the

darker vertices are more extended in space: the adhesion potential is flatter around the MM stacking, so the system explores other configurations close in energy.

Having identified the two distinct vertices in the honeycomb soliton network, we now consider the consequences for the electronic structure of the material, using scanning tunnelling spectroscopy (STS) measurements of the local density of states (LDOS). Figure 4a shows STS spectra averaged on the commensurate 2H regions of the material (far from the solitons) as a function of strain. The gap decreases with increasing strain (inset to Fig. 4a and values in Supplementary Table 1). In Fig. 4b and its inset, we compare the spectra recorded on a commensurate region (2H), a dark soliton vertex (MM) and a bright vertex (XX) at a strain of 2.5%. The most prominent feature is the presence of electronic states deep inside the gap at 75 and 175 meV in the XX vertex (main panel, Fig. 4b), which are absent for both the commensurate 2H regions as well as the MM soliton vertex (see inset for zoomed out versions of the spectra). States at similar energies are observed in all XX vertices. We note that the width of the in-gap resonances

NATURE PHYSICS LETTERS

in our spectra is large due to the relatively high temperature of our measurement. To confirm the spatially bound nature of the in-gap states, we performed spectroscopic imaging at the energy of the stronger resonance, the results of which are shown in Fig. 4c. In this image, the colour scale depicts the magnitude of the LDOS, while the simultaneously acquired topography is rendered in the 3D height map. It is clearly seen that the in-gap resonance is confined solely to the XX soliton vertex that has the higher topographic height, while it is absent on the MM vertex. The spatial width of the resonance is ~2 nm.

Besides the in-gap states, weaker resonances are present in both soliton vertices starting at the band edges (better resolved in the conduction band than in the valence band). To show the nature of these band resonances, we performed an angular average of spectra around the XX site; the angular-averaged spectra are displayed as a function of distance from the XX site in Fig. 4d for a range of energies. The conduction band edge is indicated by the arrow on this image. Spatial profiles at energies of the first four resonances in the conduction band are also displayed in Supplementary Fig. 3. The resonances within the conduction band are equally spaced by ~75 meV, and their spatial structure resembles the wavefunctions of a 2D harmonic oscillator, with alternating resonances displaying opposite parities. These features are also present in STS maps around MM crossings, but are much more attenuated in that case (Supplementary Fig. 4). Apart from the vertices, the soliton itself does not display strong spatially dependent features in the LDOS at the temperature of our measurement.

In TMDs, strain-induced pseudo-magnetic fields<sup>26,27</sup> and potentials associated with corrugations<sup>28</sup> can give rise to confined states. Spatially modulated interlayer couplings due to changes in the atomic registry also affect the position of the band edges. This effect, as well as the deformation potential<sup>29</sup>, contribute to create a smooth (on the scale of the microscopic lattice) confining potential within the solitons. Its microscopic origin is thus the same as the moiré superlattice potentially created by lattice mismatch in TMD heterobilayers, where the same kind of features in the LDOS<sup>30,31</sup> are observed. The two in-gap states, however, do not belong to this sequence of odd–even parity associated with the smooth confining potential. Instead, these electronic states are deeply confined within the bandgap, as shown above, pointing to a sharper perturbation on the atomic scale related to local registry.

Figure 4e presents a simple model for this scenario, in which these states originate from multiple scattering off a sharp stacking defect at XX soliton crossings. In TMD semiconductors, conduction and valence bands are dominated by orbitals localized on the metal sites (red, Fig. 4e). The effective hopping between these orbitals (represented by dashed green arrows) is assisted by Se orbitals (localized on blue sites in Fig. 4e). At the XX soliton vertex, the strong coupling between Se atoms sitting on top of each other can lead to passivation of their orbitals, interrupting these virtual hopping processes and mimicking the effect of a Mo vacancy. This assumption is supported by the density functional calculations presented in the Supplementary Information, which show a partial flattening of the Mo-dominated valence band in the XX stacking with respect to the preferred 2H configuration. Scattering off such a defect can transfer spectral weight from the electron-hole continuum to build resonances within the bandgap. To model this quantitatively, we used a simple tight-binding model with hopping parameters for monolayer MoSe, (ref. <sup>32</sup>; for details see Supplementary Section 7). Bonds around a single Mo atom are passivated by assuming an infinite energy on the central Mo site. Figure 4d shows the LDOS calculated at different distances from the stacking defect. Although the true experimental situation is undoubtedly more complex, this simple model reproduces the presence of two in-gap states that are localized well within the soliton vertex. The use of one or more such trapped electrons to realize optical and electrical based quantum

manipulations is an exciting new alternative to traditional lithographic and defect-based engineering of quantum states.

#### Online content

Any methods, additional references, Nature Research reporting summaries, source data, extended data, supplementary information, acknowledgements, peer review information; details of author contributions and competing interests; and statements of data and code availability are available at https://doi.org/10.1038/s41567-020-0953-2.

Received: 25 October 2019; Accepted: 1 June 2020;

Published online: 06 July 2020

#### References

- Dean, C. R. et al. Hofstadter's butterfly and the fractal quantum Hall effect in moiré superlattices. *Nature* 497, 598–602 (2013).
- 2. Li, G. et al. Observation of van Hove singularities in twisted graphene layers. *Nat. Phys.* **6**, 109–113 (2009).
- Alden, J. S. et al. Strain solitons and topological defects in bilayer graphene. Proc. Natl Acad. Sci. USA 110, 11256–11260 (2013).
- Cao, Y. et al. Unconventional superconductivity in magic-angle graphene superlattices. *Nature* 556, 43–50 (2018).
- Cao, Y. et al. Correlated insulator behaviour at half-filling in magic-angle graphene superlattices. Nature 556, 80–84 (2018).
- Yankowitz, M. et al. Tuning superconductivity in twisted bilayer graphene. Science 363, 1059–1064 (2019).
- Sharpe, A. L. et al. Emergent ferromagnetism near three-quarters filling in twisted bilayer graphene. Science 365, 605–608 (2019).
- Liu, X. et al. Spin-polarized correlated insulator and superconductor in twisted double bilayer graphene. Preprint at https://arxiv.org/pdf/1903. 08130.pdf (2019).
- Seyler, K. L. et al. Signatures of moiré-trapped valley excitons in MoSe<sub>2</sub>/WSe<sub>2</sub> heterobilayers. *Nature* 567, 66–70 (2019).
- Tran, K. et al. Evidence for moiré excitons in van der Waals heterostructures. Nature 567, 71–75 (2019).
- Jin, C. et al. Observation of moiré excitons in WSe<sub>2</sub>/WS<sub>2</sub> heterostructure superlattices. Nature 567, 76–80 (2019).
- Alexeev, E. M. et al. Resonantly hybridized excitons in moiré superlattices in van der Waals heterostructures. *Nature* 567, 81–86 (2019).
- Woods, C. R. et al. Commensurate-incommensurate transition in graphene on hexagonal boron nitride. Nat. Phys. 10, 451–456 (2014).
- Kumar, H., Dong, L. & Shenoy, V. B. Limits of coherency and strain transfer in flexible 2D van der Waals heterostructures: formation of strain solitons and interlayer debonding. Sci. Rep. 6, 21516 (2016).
- Carr, S. et al. Relaxation and domain formation in incommensurate two-dimensional heterostructures. Phys. Rev. B 98, 224102 (2018).
- Naik, M. H. & Jain, M. Ultraflatbands and shear solitons in moiré patterns of twisted bilayer transition metal dichalcogenides. *Phys. Rev. Lett.* 121, 266401 (2018).
- 17. Huang, S. et al. Topologically protected helical states in minimally twisted bilayer graphene. *Phys. Rev. Lett.* **121**, 037702 (2018).
- Yoo, H. et al. Atomic and electronic reconstruction at the van der Waals interface in twisted bilayer graphene. Nat. Mater. 18, 448–453 (2019).
- 19. Kerelsky, A. et al. Maximized electron interactions at the magic angle in twisted bilayer graphene. *Nature* **572**, 95–100 (2019).
- Ju, L. et al. Topological valley transport at bilayer graphene domain walls. Nature 520, 650–655 (2015).
- Yankowitz, M. et al. Electric field control of soliton motion and stacking in trilayer graphene. Nat. Mater. 13, 786–789 (2014).
- Jiang, L. et al. Manipulation of domain-wall solitons in bi- and trilayer graphene. Nat. Nanotechnol. 13, 204–208 (2018).
- Edelberg, D. et al. Approaching the intrinsic limit in transition metal diselenides via point defect control. Nano Lett. 19, 4731–4739 (2019).
- 24. Cooper, R. C. et al. Nonlinear elastic behavior of two-dimensional molybdenum disulfide. *Phys. Rev. B* 87, 035423 (2013).
- Pokrovsky, V. L. & Talapov, A. L. Ground state, spectrum and phase diagram of two-dimensional incommensurate crystals. Phys. Rev. Lett. 42, 65–67 (1979).
- Levy, N. et al. Strain-induced pseudo-magnetic fields greater than 300 tesla in graphene nanobubbles. Science 329, 544–547 (2010).
- Cazalilla, M. A., Ochoa, H. & Guinea, F. Quantum spin Hall effect in two-dimensional crystals of transition-metal dichalcogenides. *Phys. Rev. Lett.* 113, 077201 (2014).
- Chirolli, L., Prada, E., Guinea, F., Roldán, R. & San-Jose, P. Strain-induced bound states in transition-metal dichalcogenide bubbles. 2D Mater. 6, 025010 (2019).

LETTERS NATURE PHYSICS

- Shen, T., Penumatcha, A. V. & Appenzeller, J. Strain engineering for transition metal dichalcogenides based field effect transistors. ACS Nano 10, 4712–4718 (2016).
- 30. Zhang, C. et al. Interlayer couplings, moiré patterns, and 2D electronic superlattices in MoS<sub>2</sub>/WSe<sub>2</sub> hetero-bilayers. *Sci. Adv.* 7, e1601459 (2017).
- 31. Pan, Y. et al. Quantum-confined electronic states arising from the moiré pattern of MoS<sub>2</sub>-WSe<sub>2</sub> heterobilayers. *Nano Lett.* **18**, 1849–1855 (2018).
- Liu, G.-B., Shan, W.-Y., Yao, Y., Yao, W. & Xiao, D. Three-band tight-binding model for monolayers of group-VIB transition metal dichalcogenides. *Phys. Rev. B* 88, 085433 (2013).

**Publisher's note** Springer Nature remains neutral with regard to jurisdictional claims in published maps and institutional affiliations.

© The Author(s), under exclusive licence to Springer Nature Limited 2020

NATURE PHYSICS LETTERS

### Methods

To achieve high strains (above 1%) in situ while performing STM measurements, we constructed a novel piezoelectric device that is compatible with flag-type STM sample holders (Fig. 1b). This device is based on similar designs used recently for transport measurements under high uniaxial strain<sup>33</sup>. In brief, a sample was bridged between two stacks of piezoelectric actuators that formed the two ends of a movable bridge. By application of a voltage to the piezoelectric device, the two ends of the bridge could be moved further apart or closer together, creating uniaxial strain in the sample. Our experiments were carried out on bulk crystals of 2H-MoSe, which were glued firmly onto ruby substrates to form the ends of the strain bridge, giving the structural rigidity necessary for STM measurements. The resting separation of the ends of the bridge was 100 μm with a maximum variance of  $\pm 3$  μm under the application of a voltage (maximum uniaxial strain of  $\pm 3\%$ , beyond which sample damage occurred). Following the construction process, the sample was mechanically exfoliated in ultrahigh vacuum (UHV) conditions, immediately before the experiment, to avoid exposure to ambient. The crystal was secured at its edges and at the bottom with epoxy, and the bulk crystal was strained uniformly by application of a voltage to the piezoelectric. The experiments were conducted in a homemade STM at a temperature of 77 K, which was sufficient to avoid carrier freeze-out in the semiconducting crystals.

## Data availability

Source data are provided with this paper. All other data that support the plots within this paper and other findings of this study are available from the corresponding author upon reasonable request.

### References

 Wieteska, A. et al. Uniaxial strain tuning of superconductivity in 2H-NbSe<sub>2</sub>. Preprint at https://arxiv.org/abs/1903.05253 (2019).

# Acknowledgements

This work was supported by the National Science Foundation (NSF) via grant no. DMR-1610110 (to D.E.) and by the NSF MRSEC programme through Columbia in the Center for Precision Assembly of Superstratic and Superatomic Solids (DMR-1420634; to H.O. and A.N.P.). Support for STM measurements was provided by the Air Force Office of Scientific Research (grant no. FA9550-16-1-0601). The computational work was supported primarily by contract W911NF-16-1-0447 from the Army Research Office (to V.B.S.) and by grant no. CMMI-1727717 (to H.K.) from the NSF.

### **Author contributions**

D.E. performed STM experiments under the guidance of A.N.P. H.K. performed density functional theory and molecular dynamics simulations under the guidance of V.S. H.O. performed analytical calculations. D.E., H.O. and A.N.P. wrote the manuscript with assistance from H.K. and V.S.

## **Competing interests**

The authors declare no competing interests.

### **Additional information**

**Supplementary information** is available for this paper at https://doi.org/10.1038/s41567-020-0953-2.

Correspondence and requests for materials should be addressed to H.O. or A.N.P. Reprints and permissions information is available at www.nature.com/reprints.